

Spatially Correlated Rotary Cross-Spectral Analysis of Wave Forcing in the Surf Zone

During the RIPEX / Steep Beach Experiment, Sand City, CA

LT Micah Weltmer
20 September 2002
OC3570
Operational Oceanography

TABLE OF CONTENTS

INTRODUCTION.....3

EXPERIMENT.....4

- Data Acquisition
- Data Quality
- Data Selection

RESULTS AND DISCUSSION.....10

REFERENCES.....13

FIGURES.....14

- List of Figures
- Figures

INTRODUCTION

The RIPEX/Steep Beach Experiment was a multi-institutional effort to examine high-resolution velocity profiles, small- and large-scale morphology changes, and detailed wave measurements on a steep (1:40 or less), relatively planar beach that is characterized by frequent rip currents of the order of 1-2m/s. Contributors to the experiment were scientists from the Naval Postgraduate School, University of Florida, and Ohio State University. Measurements included a cross-shore array of PUV's and Acoustic Doppler Velocimeters (ADV's) measuring pressure and horizontal velocity components at ~8Hz, both in the rip channel and between; Acoustic Doppler Current Profilers (ADCP's) mounted seaward of the surf zone measuring 2-second velocities in 25cm vertical bins; a vertical tower array, mounted in the surf zone between rip channels, of Electromagnetic Current Meters (ECM's) measuring u, v, and w velocity components at ~4Hz; a capacitance wave wire mounted on the same tower; and a 'goal post' frame mounted in the surf zone near the tower that contained a Bistatic Coherence Doppler Velocity and Sediment Profiler (BCDVSP), acoustic point altimeter, acoustic scanning altimeter and an underwater camera.

Sand City was chosen for the site of this experiment for its predominance of rip currents and the moderate wave energy compared to a steeper, more exposed site such as Fort Ord (Figure 1). Instruments were placed in an array that extended to approximately 200m offshore, to a depth of approximately 6 meters (Figure 2). Data recording began on 14 April 2001 and continued to 15 May 2001. The data set is relatively complete, with the exception of instruments in the surf zone or shoreward that would emerge from the water at low tides (e.g., ECM's and the wave wire on the tower). This study will examine near-bed velocity measurements in the surf

zone and seaward both in the rip channel and between channels. Using complex rotary spectra, the coupling between on- and off-shore, rip channel and non-rip channel wave forcing will be shown. A vertical coupling will be shown for the offshore ADCP measurements for demonstrations purposes.

EXPERIMENT

Data acquisition

All instruments in RIPEX/Steep Beach were connected by coaxial cable to a central collection site at the Beach Station on Del Monte Beach. ADCPs measure up to 30 25cm vertical bins of horizontal velocity at 2-second intervals. ADVs and PUVs measure pressure and horizontal velocity components at 8Hz at a point near the bottom, and the ECMs measure point 3D velocity components at 4Hz. The tower contained 7 ECMs which were mounted from 14cm to 2.4m off the bed. Future study will focus on the bottom forcing and its influence on changes in morphology in the surf zone. For this reason, the second ADCP bin (~1.5m above the bed) and lowest ECM (~14 cm above the bed) have been chosen for this analysis. Vertical coupling will be shown using a comparison between the ADCP velocities from the second and fourth (~2m above the bed). This will ensure enough separation to demonstrate bottom boundary layer effects, but not so much as to make the upper bin be located out of the water.

Data Quality

Prior to spectral analysis of any kind, data quality must be ensured. Specifically, the data must be 1) continuous, 2) free of large errors, and 3) of uniform sampling frequency.

Although data gaps did occur during the experiment, all of the data used for this study is continuous for the period being examined. Even so, a routine was employed to replace any data gaps with the overall mean. This method has little overall effect on the spectral analysis because any spectral analysis begins by detrending the data with a linear scheme.

Large errors in velocity data can cause tremendous problems with a spectral analysis, complex rotary spectral analysis being no exception. Large errors can be conservatively defined by a deviation of greater than 3σ from the mean, that persists for no more than 5 data points (~10 seconds). A linear interpolation “de-spiking” routine was thus employed to remove such large errors from the component data, yet preserve the overall form of the data.

Finally, the data had to be of uniform sampling times in order for a comparative spectral analysis to be valid. While the PUVs and ADVs sampled at 8Hz and the ECMs at 4Hz, the ADCP data was only recorded at ~0.5Hz. Interpolation to a higher frequency would not increase the resolution of the data, so higher frequency data (PUV, ADV, ECM) was instead reduced to the lowest frequency (0.5Hz) using a linear interpolation scheme. The higher frequency measurements were sub-sampled at the times of the ADCP data, resulting in four sets of velocity measurements of exactly the same size and sample times.

Instruments were installed as nearly orthogonal to the shoreline as possible, allowing the use of a shore-normal coordinate system (Figure 3) to eliminate reference and directional corrections that must be made in an open-water data set. Interestingly, however, the rotary spectral analysis, which will be outlined below, removes coordinate rotation errors that may remain, making adjustments unnecessary in any case. Figure 4 shows what the cleaned data looks like in two different representations

Data Selection

Examination of summary data for the entire experiment revealed that a high-wave-energy event occurred during 22 April 2001, prior to which the morphology as shown by the BACVSP and scanning acoustic altimeter was characterized by large (~10cm), short-wavelength (~30cm) ripples, but after which the bed remained nearly planar (Figure 5). This study will focus on two days, one before and one after the event, in order to evaluate the spectral signal which either triggers or characterizes the respective morphology regimes. In the interest of data consistency, 2.4-hour high tide periods on day 110 and 113 (Figure 6) were compared. Larger time series (days 109-112, days 112-114) were examined to show the relative energy of the high frequency forcing (wind waves, infragravity) and the lower frequency forcing (inertial, tidal).

Rotary Cross-Spectral Analysis

Rotary cross-spectral analysis allows for a statistical measure of coherence and phase relationship between two vector time series, without the confusion of four correlation coefficients that standard cross-spectral analysis of two scalar series yields. Additionally, rotary spectral analysis is independent of coordinate rotation, whereas scalar correlation coefficients would vary.

For rotary spectral analysis, velocity components u and v are combined into a complex vector $w_x = u_x + iv_x$. These complex velocities are decomposed into anticlockwise and clockwise motions, and transformed into positive and negative frequencies, respectively. The following excerpt from Blodgett (2002) summarizes the rotary spectral analysis derived by Mooers (1973).

As an example, consider two vector time series (current velocity (c) and wind velocity (w)) defined by:

$$\begin{aligned} w_c &= u_c + iv_c \\ w_w &= u_w + iv_w \end{aligned} \quad (1)$$

respectively. Taking the Fourier transform of both the current and wind complex time series yields:

$$W(f) = \begin{cases} A^+ e^{-i\theta^+}, & f \geq 0 \\ A^- e^{-i\theta^-}, & f \leq 0 \end{cases} \quad (2)$$

Equation 2 associates the negative frequencies with the clockwise rotary components and the positive Fourier transform frequencies with the anticlockwise rotary components.

Inner cross-spectrum: The inner cross-spectrum $S_{cw}(f)$ compares the joint energy of the current and wind time series for the rotary components rotating in the same direction (e.g. the clockwise component of the wind vector to the clockwise component of the near-surface current vector)

$$\begin{aligned} S_{cw}(f) &= \langle W_c^*(f) W_w(f) \rangle \\ &= \begin{cases} A_c^+(f) A_w^+(f) e^{-i(\theta_c^+ - \theta_w^+)}, & f \geq 0 \\ A_c^-(f) A_w^-(f) e^{-i(\theta_c^- - \theta_w^-)}, & f \leq 0 \end{cases} \end{aligned} \quad (3)$$

with * denoting the complex conjugate and $\langle \bullet \rangle$ representing an ensemble average.

Inner autospectrum: The autospectrum for each time series is then:

$$S_{cc} = \begin{cases} [A_c^+(f)]^2, & f \geq 0 \\ [A_c^-(f)]^2, & f \leq 0 \end{cases} \quad (4)$$

$$S_{ww} = \begin{cases} [A_w^+(f)]^2, & f \geq 0 \\ [A_w^-(f)]^2, & f \leq 0 \end{cases} \quad (5)$$

Thus, as an example, $S_{cc}(f \geq 0)$ is the power spectral density of the anticlockwise component of the current time-series. The area under this curve versus frequency will therefore equal the variance of the cross-shore and along-shore current velocity components.

Inner coherence squared: The inner coherence-squared between the wind and current time series at frequency (f) is calculated according to:

$$C_{cw} = \begin{cases} \left\{ \left\langle A_1^+ A_2^+ \cos(\theta_1^+ - \theta_2^+) \right\rangle^2 + \left\langle A_1^+ A_2^+ \sin(\theta_1^+ - \theta_2^+) \right\rangle^2 \right\} / \left\langle A_1^{+2} \right\rangle \left\langle A_2^{+2} \right\rangle, f \geq 0 \\ \left\{ \left\langle A_1^- A_2^- \cos(\theta_1^- - \theta_2^-) \right\rangle^2 + \left\langle A_1^- A_2^- \sin(\theta_1^- - \theta_2^-) \right\rangle^2 \right\} / \left\langle A_1^{-2} \right\rangle \left\langle A_2^{-2} \right\rangle, f \leq 0 \end{cases} \quad (6)$$

The coherence C_{cw} ranges from 0 to 1, and represents the similarity (or variability) of the two time series to each other. A value near unity indicates a high degree of correlation, while a coherence near zero indicates a negligible correlation. Using a 95% confidence interval, equation 7 provides a limiting value, or level to which coherence-squared values occur by chance:

$$C_{cw}^{significant} = 1 - 0.5^{[2/(DOF-2)]} \quad (7)$$

where DOF represents the degrees of freedom contained in the time-series.

Inner phase: The phase for the cross spectrum and coherence measures the phase lead of the rotary component of the current time-series with respect to the wind time-series. It can be calculated according to the following equation:

$$\tan(\phi_{cw}) = \begin{cases} \left\{ \left\langle A_c^+ A_w^+ \sin(\theta_c^+ - \theta_w^+) \right\rangle^2 / \left\langle A_c^+ A_w^+ \cos(\theta_c^+ - \theta_w^+) \right\rangle^2 \right\}, f \geq 0 \\ \left\{ \left\langle -A_c^- A_w^- \sin(\theta_c^- - \theta_w^-) \right\rangle^2 / \left\langle A_c^- A_w^- \cos(\theta_c^- - \theta_w^-) \right\rangle^2 \right\}, f \leq 0 \end{cases} \quad (8)$$

Outer cross-spectrum: The outer cross-spectrum $O_{cw}(f)$ compares the joint energy of the current and wind time series for the rotary components rotating in the opposite direction (e.g. the clockwise component of the wind vector to the anticlockwise component of the near-surface current vector).

$$O_{cw}(f) = \langle W_c(-f)W_w(f) \rangle \\ = \begin{cases} A_c^-(f)A_w^+(f)e^{[i(\theta_c^+ - \theta_w^-)]}, f \geq 0 \\ A_c^+(f)A_w^-(f)e^{[i(\theta_c^- - \theta_w^+)]}, f \leq 0 \end{cases} \quad (9)$$

Outer autospectrum: The outer rotary autospectrum for each time series is then:

$$O_{cc} = A_c^-(f)A_c^+(f)e^{[i(\theta_c^+ - \theta_c^-)]}, f \geq 0 \quad (10)$$

$$O_{ww} = A_w^-(f)A_w^+(f)e^{[i(\theta_w^+ - \theta_w^-)]}, f \geq 0 \quad (11)$$

Both outer power spectral densities are symmetric about $f=0$.

Outer coherence squared: The outer coherence squared between the wind and current time series at frequency (f) is calculated according to:

$$D_{cw} = \begin{cases} \left\langle A_c^- A_w^+ \right\rangle \left[\left\langle \cos(\theta_w^+ - \theta_c^-) \right\rangle^2 + \left\langle \sin(\theta_w^+ - \theta_c^-) \right\rangle^2 \right] / \left\langle A_w^{+2} \right\rangle \left\langle A_c^{-2} \right\rangle, f \geq 0 \\ \left\langle A_c^+ A_w^- \right\rangle \left[\left\langle \cos(\theta_c^+ - \theta_w^-) \right\rangle^2 + \left\langle \sin(\theta_c^+ - \theta_w^-) \right\rangle^2 \right] / \left\langle A_c^{+2} \right\rangle \left\langle A_w^{-2} \right\rangle, f \leq 0 \end{cases} \quad (12)$$

Outer phase: The phase for the outer cross-spectrum and coherence is given by:

$$\tan(\psi_{cw}) = \begin{cases} \left\{ \left\langle A_c^- A_w^+ \sin(\theta_c^- - \theta_w^+) \right\rangle / \left\langle A_c^- A_w^+ \cos(\theta_c^- - \theta_w^+) \right\rangle \right\}, f \geq 0 \\ \left\{ \left\langle A_c^+ A_w^- \sin(\theta_c^+ - \theta_w^-) \right\rangle / \left\langle A_c^+ A_w^- \cos(\theta_c^+ - \theta_w^-) \right\rangle \right\}, f \leq 0 \end{cases} \quad (13)$$

Example Calculations

In order to better illustrate the execution of this methodology, two counter-rotating circular sinusoidal waves of equal magnitude were generated with superimposed noise (Figure 7). After the complex rotary cross-spectral analysis was conducted, the inner autospectra of each component (Figure 8) and the inner cross-spectral density (Figure 9) were plotted versus frequency. Figure 8 clearly shows that all of the energy in the first signal (designed for anticlockwise rotation) does indeed reside in the positive frequency realm. Likewise, all of the energy in the second signal (clockwise rotation) can be found in the negative frequency range. The outer cross-spectral energy plot in figure 9 shows that both the clockwise and anticlockwise energy are equal in magnitude, as expected from the original wave design.

(Blodgett, 2002)

The goal of the investigation is to examine the spatial coupling between the ADCP spectra and the other velocity measurement devices. This coupling would allow for greater understanding of how the existence or absence of rip currents alters this coupling, or simply how varying wave environments alter the coupling. Further investigation could lead to prediction of nearshore waves, rotations, and bed morphology changed from data obtained via offshore wave buoys or beyond.

RESULTS AND DISCUSSION

Examination of the long time series pressure data (Figure 10) shows high energy in the tidal range, with a secondary mode in the wind-wave and swell band. Coriolis frequency f is not expected to be a dominant energy source because of the short time and length scales of motion in the nearshore, and an associated energy peak is not observed in figure 10. Comparison of the day 112-114 power spectrum with the 109-112 day spectrum shows a substantial increase in infragravity energy, which appears to be characteristic of post-storm conditions. Autospectra of the 2.4-hour series similarly reflect the increase in infragravity energy.

Rotational spectral analysis was performed for 2.4-hour periods on both day 110 and 113 to examine wave conditions before and after the storm and its associated morphology change. Vertical variation of velocity between bins 2 and 4 of the ADCP data are compared to examine basic boundary layer effects, and lateral variation between the ADCP and EM Current Meter, PUV, and ADV to examine cross-shore and along-shore coherence.

Vertical autospectra (Figure 11) show clearly the increase in infragravity energy, and also the broader-banded swell peak after the event. Also seen is the slight displacement toward higher energy across the spectrum of the velocities higher in the water column (w4). This is due to the bottom boundary layer effects, which damp the oscillations lower in the water column. Despite these boundary layer effects, the slab-like motion of waves in shallow water produce high coherences and low phase lags, especially in the swell and high-infragravity (~surf beat) bands (Figure 11c-11f).

Spatial auto spectra again reflect the increased infragravity energy after the storm. Coherences are expected to be marginal in the cross-shore (PUV) and along-shore (ADV) directions, while the diagonal coherence (ECM) is not expected to be significant due to the

complex bathymetry, wave transformation, wave reflection, and convergence. Curiously, however, spectral coherence in any lateral direction is not significant at any frequency (Figure 12). An extremely narrow band is seen to just break the 95% significance threshold (Figure 12b) at the highest swell peak frequency, but nowhere else. This is much less coherence than expected.

Viewing the outer (cross-rotating) coherences, however, showed significant coupling at various bands throughout the spectrum (not shown). Outer cross-spectra showed two distinct peaks at surf beat (infragravity, $T \sim 15$ sec) and swell ($T \sim 10$ sec) frequencies. The clockwise rotation of the ADCP was correlated well with the anticlockwise rotation of the other instruments at the surf beat frequency, and vice versa was observed at the swell frequencies. This result was seen in the cross-shore, alongshore, and diagonal directions alike. This unusual result was not expected and could be the result of improper decimation of the high frequency data.

If this result is valid, however, it shows a significant correlation in the cross-rotational energies of the ADCP and the other instrument locations. This could be a function of the relative position of each instrument with respect to the rip currents. The ADCP and the PUV, located in the same rip channel, would be positioned on opposite ends of the rip current, with the PUV at the origin and the ADCP at the end of the flow. This results in the expected coupling, but the cross-rotational nature of the coherence indicates that the rip current flows diagonally between the instrument locations, putting each under the influence of adjacent, counter-rotating circulations. Likewise, the ECM and ADV are both on the far side of the bar and under the influence of the next rip current to the south, also imposing a counter-rotational coupling with the ADCP. The disparate frequencies of the cross-spectral peaks would indicate that the swell-induced circulation within the rip cell was counter to that induced by the surf beat. Why the

direction of origin for these two waves would be difference, one can only speculate, but the difference is obviously significant enough to force directly opposing, fairly energetic nearshore circulations.

These results are highly questionable due to the unexpected nature. Further investigation should focus on time-variant changes in the co-rotational and counter-rotational coupling to assess the application to wave and bottom forcing. Also in question is the decimation method used to put the data sets into similar sample rates. This could account for error in a minor sense, or could drastically alter or even reverse the findings of this study.

REFERENCES

- Blodgett, W. C., 2002: Rotary cross-spectral analysis of low frequency currents with co-located wind measurements in the southern Monterey Bay. Class project, OC3570 Operational Oceanography.
- Mooers, C.N.K. 1973: A technique for the cross spectrum analysis of pairs of complex-valued time series, with emphasis on properties of polarized components and rotational invariants. *Deep-Sea Res.*, 20, 1129-1141.

LIST OF FIGURES

Figure 1. Aerial photograph of Sand City beach, showing active rip currents regularly spaced along the shore.

Figure 2. RIPEX instrument locations. Blue is ADV, Red is PUV, and Black is ADCP. The green "X" approximates tower and goalpost location.

Figure 3. Cross-Shore Normal Coordinate System off Sand City Beach in Monterey Bay, CA.

Figure 4. a) Component and b) vector representation of cleaned day 110 ADCP data. (Not available due to /w drive error.

Figure 5. Gridded bathymetry of 1.2m x 1.2m footprint of XY Altimeter, showing a) day 110, before the storm, and b) day 114, after the storm.

Figure 6. Tidal data from the RIPEX period. Red bars delimit high tide periods examined.

Figure 7. Two randomly generated counter-rotating circular sinusoidal waves of equal magnitude.

Figure 8. Inner autospectra output from rotary analysis of randomly generated circular waves.

Figure 9. Outer cross spectrum output from rotary analysis of randomly generated circular waves.

Figure 10. Pressure spectra measured by the ADCP for the periods a) day 109-112, before the storm, and b) day 112.5-114.5, after the storm.

Figure 11. Rotary spectral analysis of bins 2 & 4 (1.5 and 2.0m above the bed, respectively) over a 2.4-hour period: a), b) autospectra on days 110 and 113; c), d) frequency coherence for the same periods; e), f) frequency phase lag for the same periods.

Figure 12. Rotary a) autospectra and b) coherence of day 110 and 114 ADCP and PUV data.

Figure 13. Inner autospectra, outer cross-spectra, and outer coherence of ADCP and PUV data, day 110. (Not shown due to w/ drive error)



Figure 1. Aerial photograph of Sand City beach, showing active rip currents regularly spaced along the shore.

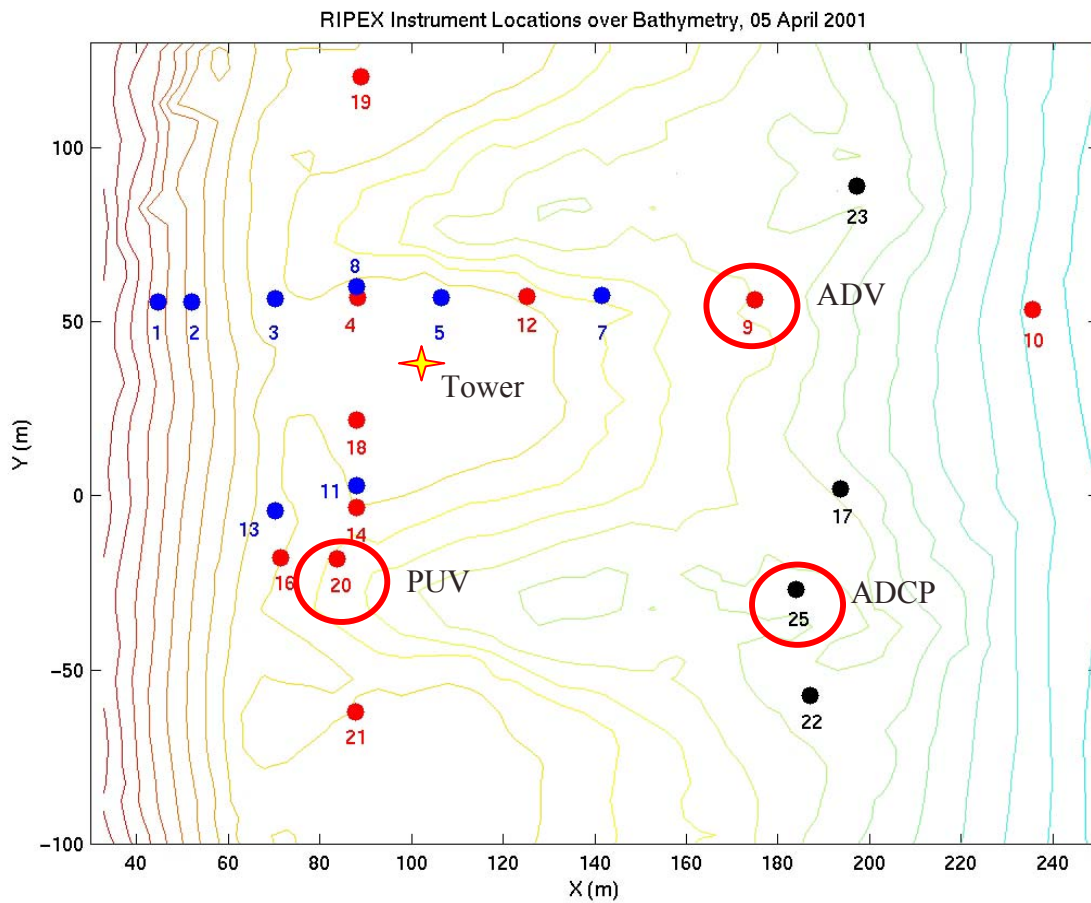


Figure 2. RIPEX instrument locations. Blue is ADV or pressure sensor, Red is PUV, and Black is ADCP. The green “X” approximates tower and goalpost location.

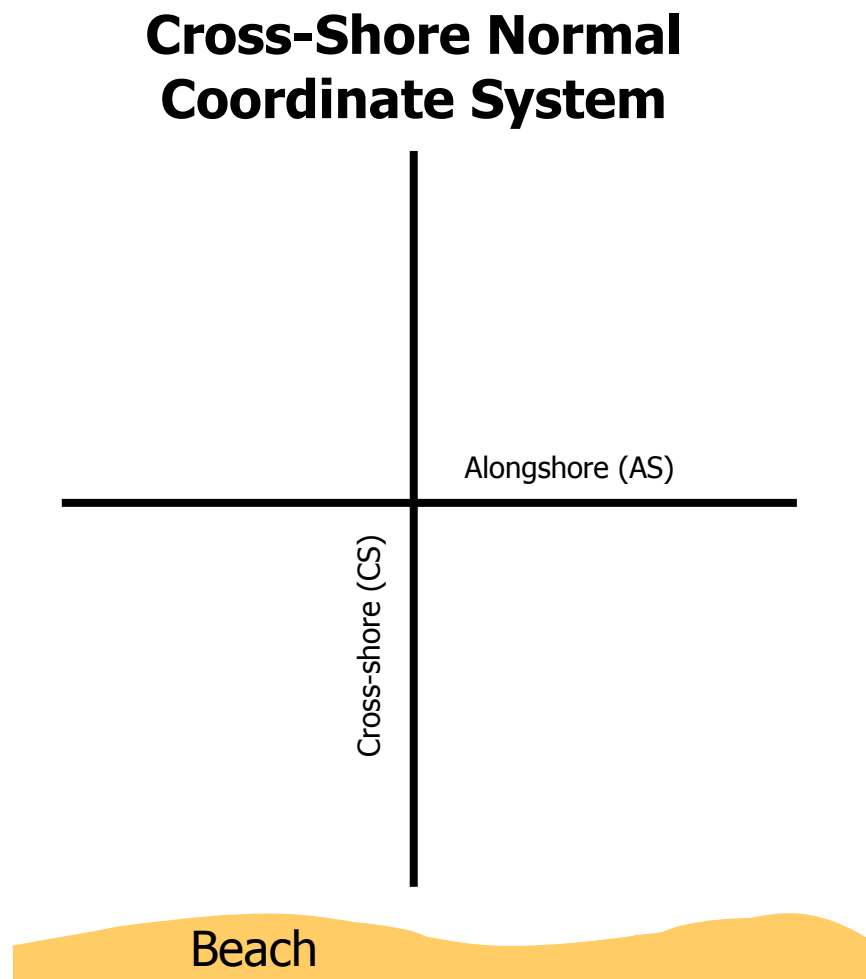
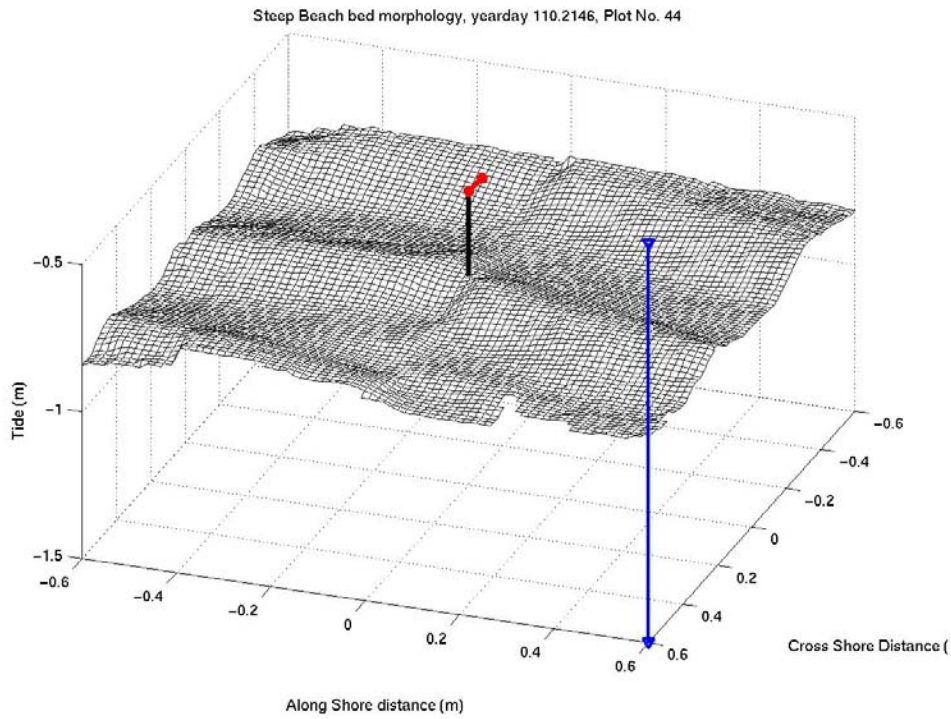
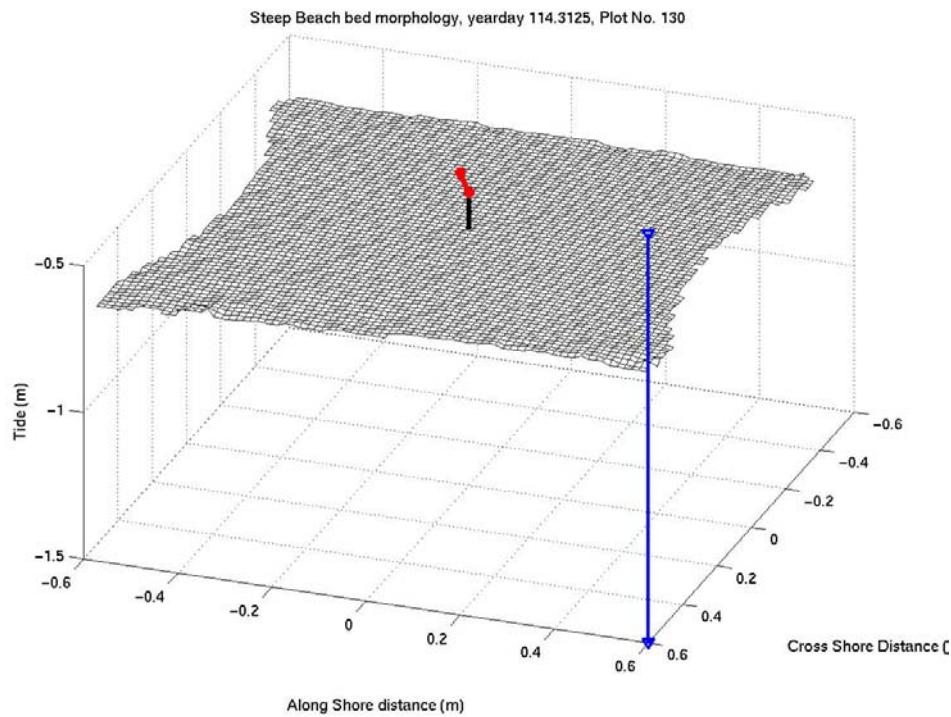


Figure 3. Cross-Shore Normal Coordinate System off Sand City Beach in Monterey Bay, CA.

Figure 4. a) Component and b) vector representation of cleaned day 110 ADCP data. (Not available due to /w drive error.



a)



b)

Figure 5. Gridded bathymetry of 1.2m x 1.2m footprint of XY Altimeter, showing a) day 110, before the storm, and b) day 114, after the storm. Red bar above bed denotes mean current, blue stick in near corner denotes mean η (sea surface height).

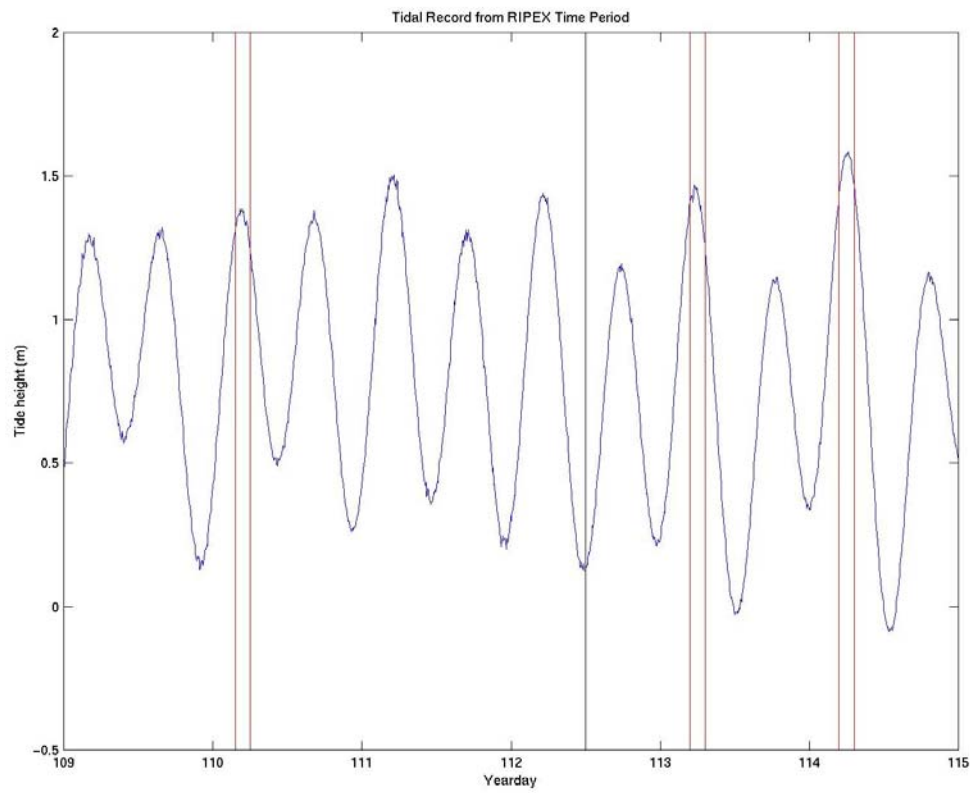


Figure 6. Tidal data from the RIPEX period. Red bars delimit high tide periods examined.

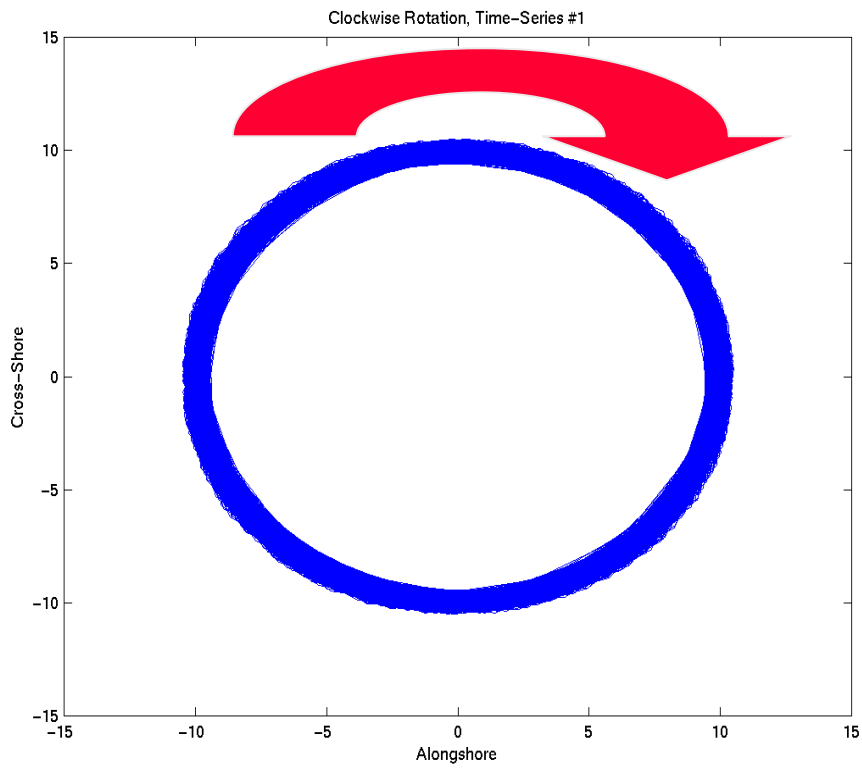
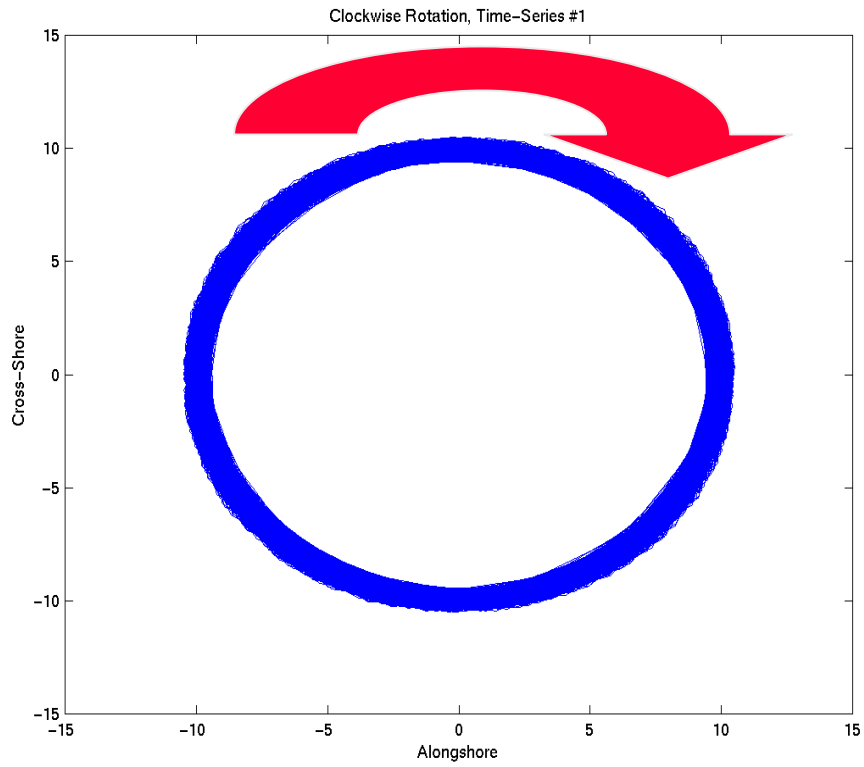


Figure 7. Two randomly generated counter-rotating circular sinusoidal waves of equal magnitude.

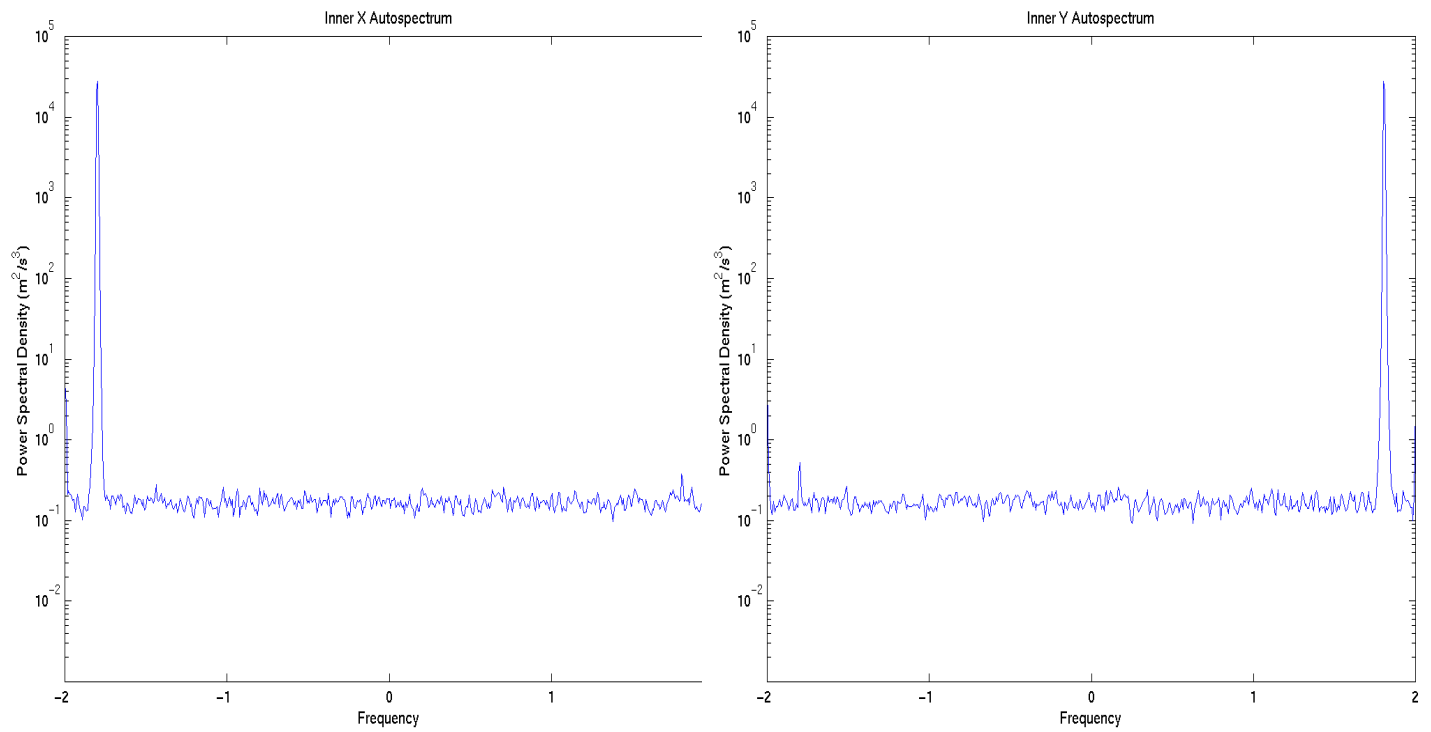


Figure 8. Inner autospectra output from rotary analysis of randomly generated circular waves.

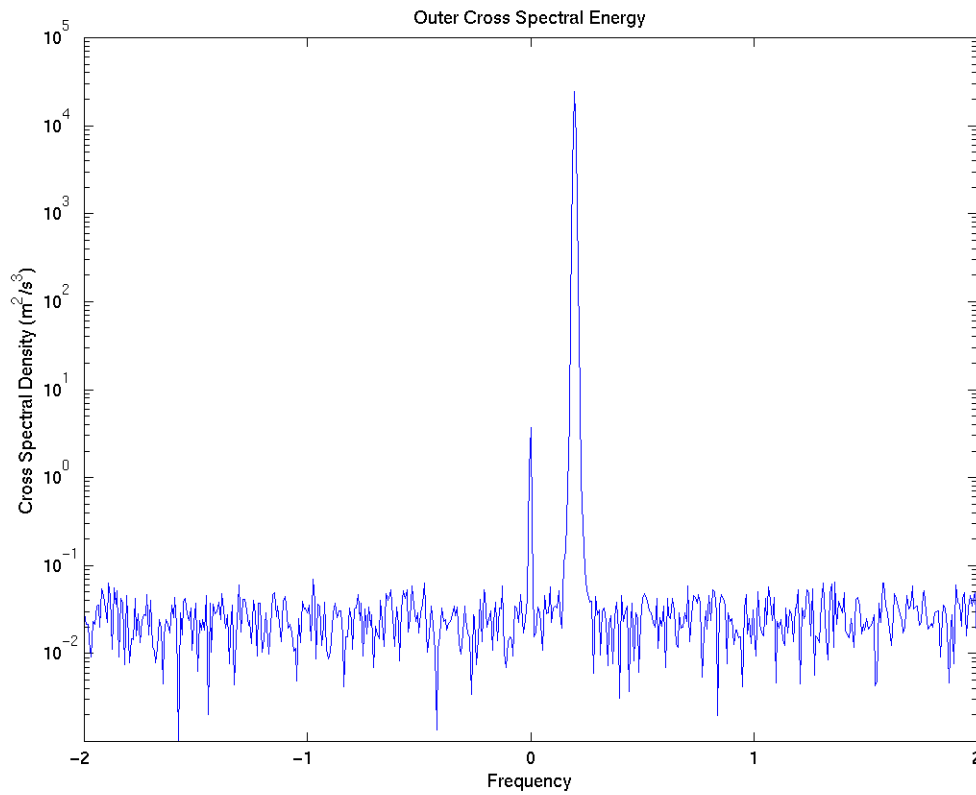


Figure 9. Outer cross spectrum output from rotary analysis of randomly generated circular waves.

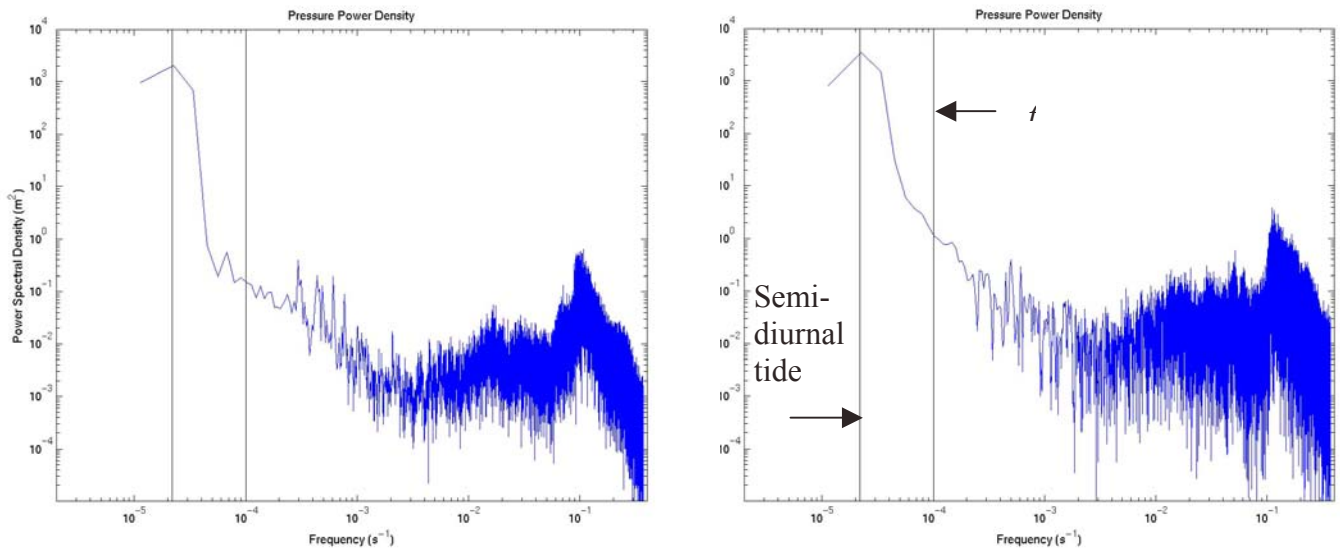


Figure 10. Pressure spectra measured by the ADCP for the periods a) day 109-112, before the storm, and b) day 112.5-114.5, after the storm.

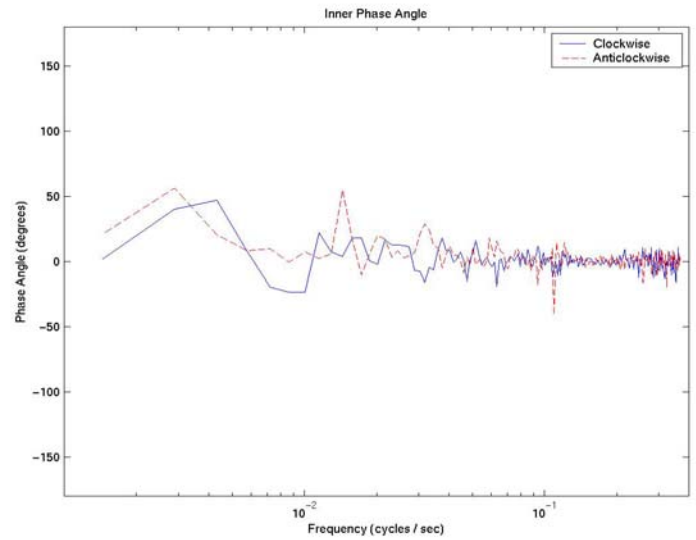
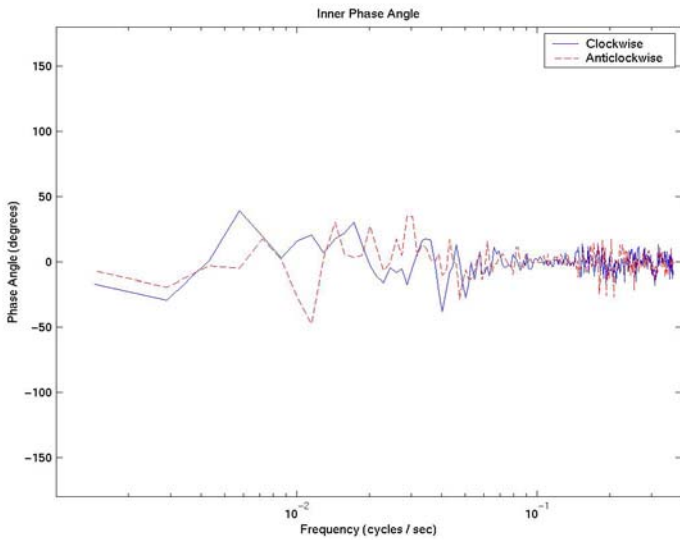
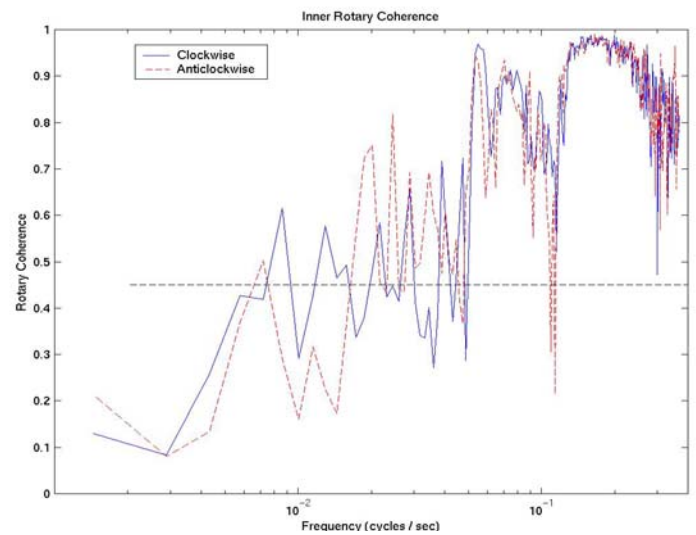
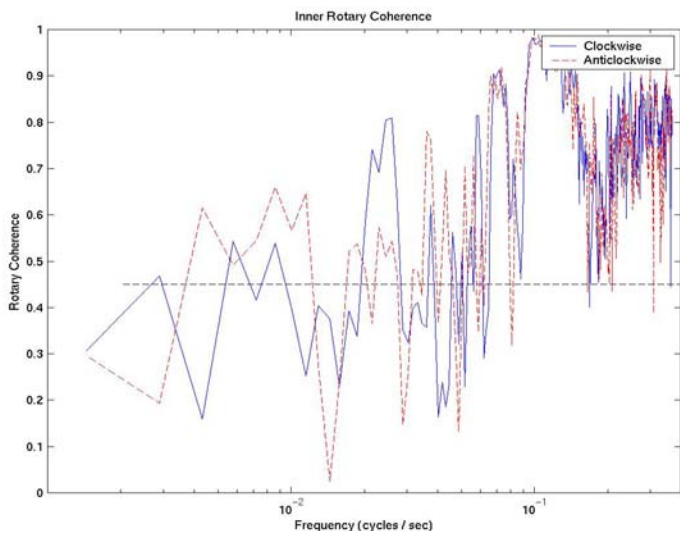
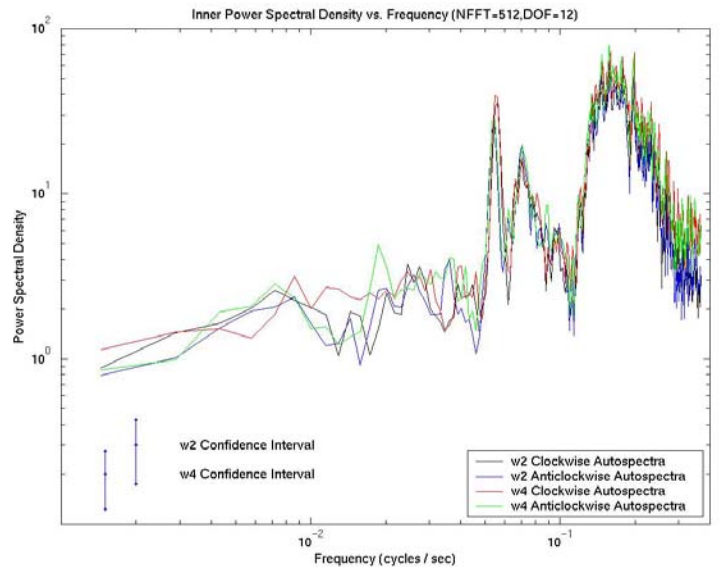
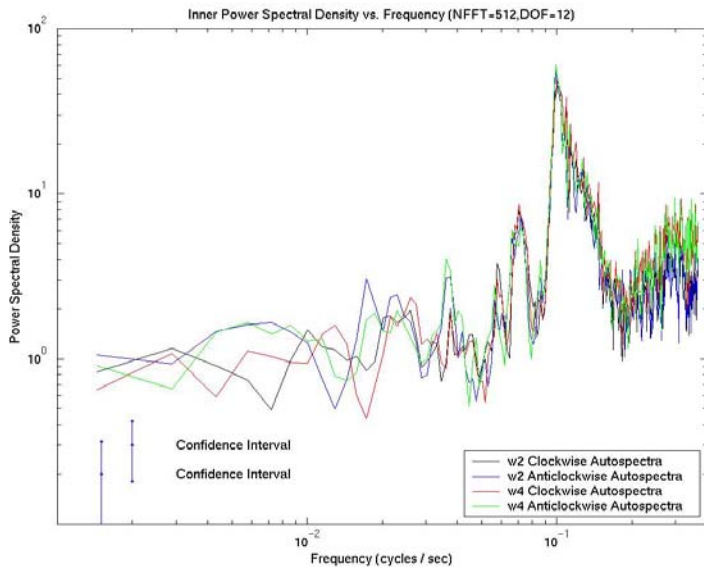


Figure 11. Rotary spectral analysis of bins 2 & 4 (1.5 and 2.0m above the bed, respectively) over a 2.4-hour period: a), b) autospectra on days 110 and 113; c), d) frequency coherence for the same periods; e), f) frequency phase lag for the same periods.

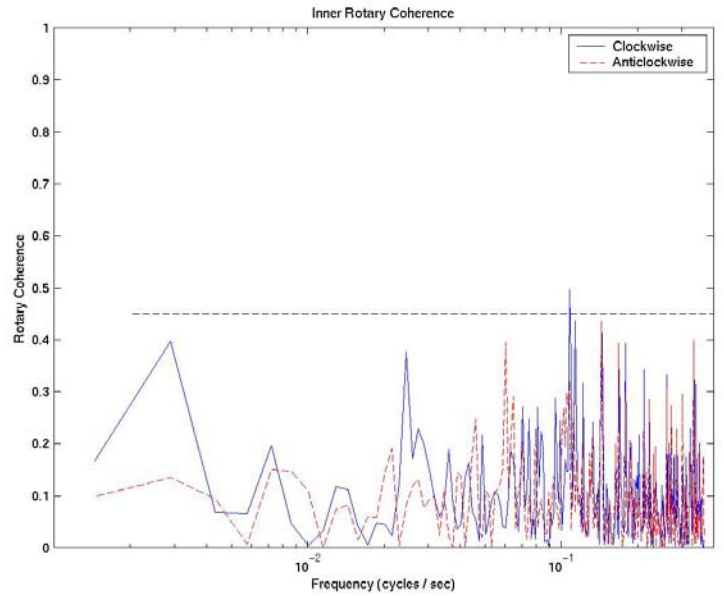
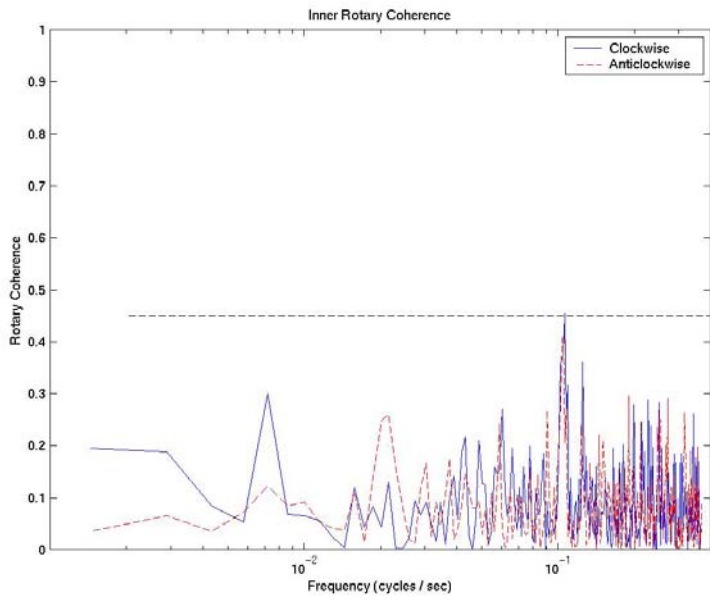
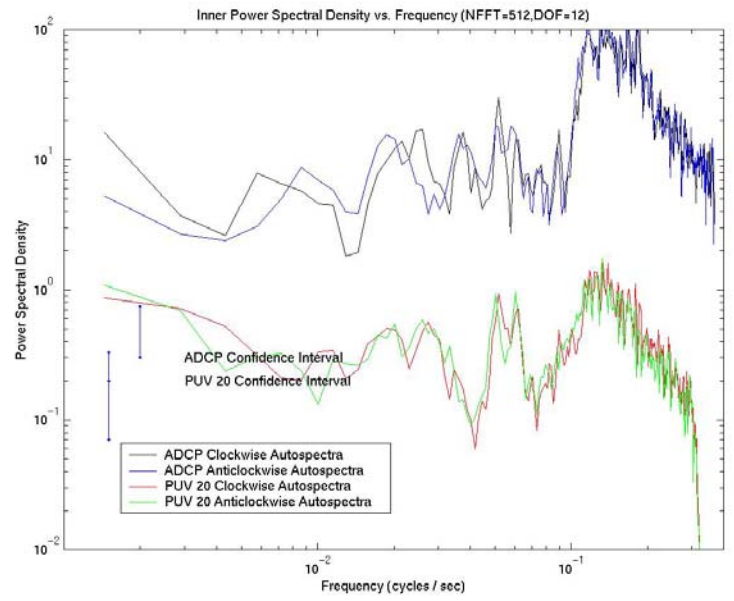
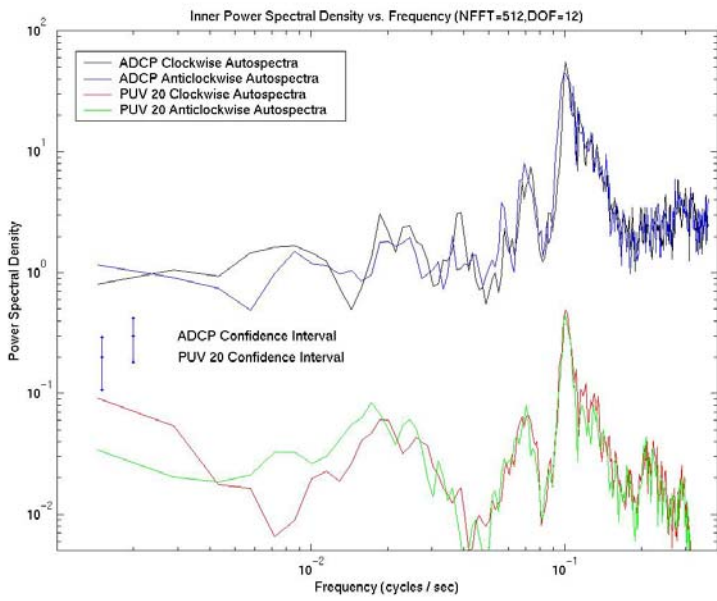


Figure 12. Rotary (top) autospectra and (bottom) coherence of day 110 and 114 ADCP and PUV data.

Figure 13. Inner autospectra, outer cross-spectra, and outer coherence of ADCP and PUV data, day 110. (Not shown due to w/ drive error)